To what extent are the IASI and ERA5 water vapour profiles representative of the conditions in the autumn 2022 during the WaLiNeAs field campaign

Patrick Chazette[1], Andreas Behrendt[2], Adolfo Comerón[3], Paolo Di Girolamo[4], Marco Di Paolantonio[4,5], Davide Dionisi[5], Cyrille Flamant[6], José Luis Gómez-Amo[7], Jérémy Lagarrigue[1], Frédéric Laly[1,8], Diego Lange[2], Constantino Muñoz-Porcar[3], Alejandro Rodríguez-Gómez[3], Michaël Sicard[3,9], Donato Summa[10], Julien Totems[1], María Pilar Utrillas[7], Pedro C. Valdelomar[7], Volker Wulfmeyer[2]

[1]Laboratoire des Sciences du Climat et de l'Environnement (LSCE), UMR8212, Laboratoire mixte CEA-CNRS-UVSQ, CEA Saclay, 91191 Gif-sur-Yvette, France
[2]Institut Fur Physik Und Meteorologie, Universitat Hohenheim, Stuttgart, Germany
[3]CommSensLab, Department of Signal Theory and Communications, Universitat Politecnica de Catalunya (UPC), Barcelona, Spain
[4]Dipartimento di Scienze della Salute, Universita degli Studi della Basilicata, Potenza, Italy
[5]Institute of Marine Sciences, National Research Council, Rome, Italy
[6]LATMOS/IPSL, CNRS-SU-UVSQ, Sorbonne Université, Paris, France
[7]Solar Radiation Group, Department de Física de la Terra i Termodinàmica, Universitat de València, Spain
[8]ADDAIR Company, 78530, Buc, France
[9]LACy, Laboratoire de l'Atmosphère et des Cyclones UMR 8105 CNRS, Université de La Réunion, Météo-France, Saint-Denis, Réunion, France
[10]Institute of Methodologies for Environmental Analysis, National Research Council, Tito Scalo, Italy

Correspondence to: Patrick Chazette (Patrick.chazette@lsce.ipsl.fr)

Keywords: Raman, Lidar, IASI, ERA5, Water vapour, WaLiNeAs

Abstract. The WaLiNeAs campaign took place along the north-western Mediterranean coast between October 2022 and January 2023. This period was marked by unusual weather conditions associated with dry autumn and winter. In such conditions and for the first time, eight ground-based stations equipped with water vapour Raman lidars were strategically deployed by four European countries. We studied the consistency of this network with the water vapour mixing ratio (WVMR) products derived from the Infrared Atmospheric Sounding Interferometer (IASI) and the European Centre for Medium-Range Weather Forecasts (ECMWF) Reanalysis (ERA5), which assimilate IASI radiances. The statistical metrics used in the comparison are the mean bias (MB, defined as lidar – IASI or ERA5), the root mean square error (RMSE) and the correlation coefficient (COR). A positive MB of approximately ~0.4 g kg^{-1} (respectively ~0.2 g kg^{-1}) between 0.2 and 5 km above mean sea level (a.m.s.l.) indicates a systematic underestimation of the WVMR by IASI (respectively ERA5). RMSE values range from 1 to 2 g kg^{-1} across all lidar stations for IASI and ERA5, while the measurement uncertainties of the lidars are typically below 0.4 g kg^{-1}. COR presents little variation between stations; it ranges from 0.7 to 0.8 and remains almost constant between 0.2 and 5 km a.m.s.l. Both the IASI and the ERA5 products appear to accurately reproduce the temporal variability of the vertical structure of water vapour in the low troposphere. Nevertheless, they show MB and RMSE significantly above the uncertainties of lidar measurements.

1 Introduction

The Infrared Atmospheric Sounding Interferometer (IASI) has been on board the polar-orbiting MetOp (Meteorological Operational) meteorological satellites since 19 October 2006. These satellites form the space segment of the Exploitation of Meteorological Satellites (EUMETSAT) Polar System (EPS). Three generations of the IASI instrument (A to C) have been launched, with the latest being launched on 7 November 2018 and are still operational. This article uses data from the latest generation. The main mission of IASI is operational meteorology (Zhou et al., 2009). The infrared spectra measured by IASI are used directly in variational assimilation for weather forecasting (Hilton et al., 2009, 2012b; Xu et al., 2013; Matricardi and Mcnally, 2014; Heilliette et al., 2013). Alongside the assimilation of radiances, vertical profiles of water vapour mixing ratios (WVMR) are derived directly from infrared radiances on a global scale (Carissimo et al., 2005; Schlüssel et al., 2005; Schneider et al., 2010; Amato et al., 2009). The vertical distribution of WVMR is obtained using spectral intervals that are selected to ensure their weight functions are homogeneously distributed in the atmosphere. The operational IASI product offers significant scientific value for near-real-time monitoring of humidity field evolution. In particular, it is well suited for process studies of extreme precipitation events (Chazette et al., 2016) and for investigations of deep convection (Lacour et al., 2018).

Although the Level–2 water vapour product of IASI has received little validation, it could play a key role in improving our understanding of frontogenesis, convection (Held and Soden, 2000), cloud formation and aerosol hydration (Rood et al., 1987; Randriamiarisoa et al., 2006). Indeed, atmospheric water vapour acts as an energy reservoir, exchanging energy with both the atmosphere and the surface via condensation and evaporation processes involving latent heat flux. These processes all play an important role in the current context of climate change (IPCC, 2022). While the literature describes some validation exercises using radiosondes (Pougatchev et al., 2009; Divakarla et al., 2009), other authors present lidar as an excellent candidate for validating IASI water vapour products (Masiello et al., 2013). However, these comparisons were performed using only six lidar profiles. The most recent work on validating IASI-derived WVMR vertical profiles was conducted over the Mediterranean as part of the international Hydrological Cycle in the Mediterranean eXperiment (HyMeX) and Chemistry-Aerosol Mediterranean Experiment (ChArMEx) programmes (Chazette et al., 2014a). Raman lidar measurements were taken on the island of Menorca (Balearic Islands, Spain). A total of around 30 coincidences were obtained during autumn 2012 for HyMeX and summer 2013 for ChArMEx. While this work was more statistically representative, it did not incorporate the spatial variability of water vapour or assess biases. Furthermore, significant biases were revealed through comparisons between the European Centre for Medium-Range Weather Forecasts (ECMWF) Reanalysis (ERA5) (https://cds.climate.copernicus.eu/, last access: 13 August 2025), which assimilates IASI radiances (Hersbach et al., 2020), and vertical lidar profiles (Laly and Chazette, 2025). These biases could exceed 2 g kg^{-1} in the first three kilometres of the atmosphere and, under heatwave conditions, ~3 g kg^{-1} in the free troposphere. The biases must be corrected before any IASI data can be used in weather forecasts. The same applies to the future assimilations of lidar measurements (Hilton et al., 2012b; Fourrié et al., 2019). It should be noted that current knowledge suggests that lidar and IASI measurements could complement each other, with lidar compensating for IASI's lack of lower-layer sampling.

The WAter Vapor LIdar NEtwork Assimilation (WaLiNeAs) project (Flamant et al., 2021) provides an opportunity to improve the knowledge on the complementarity between the IASI- and lidar-derived WVMR profiles in the low troposphere. The field campaign, which took place from October 2022 to January 2023, was conducted across the coastal north-western Mediterranean area. It was used to compile an unparalleled database (Laly et al., 2024) of vertical WVMR profiles at eight sites equipped with Raman lidar. These sites were located between the westernmost site in Valencia (Spain) and the easternmost site in Ajaccio (Corsica, France), passing through Toulon (France) (Di Girolamo et al., 2025), to sample the upstream conditions of extreme precipitation phenomena initiated by the advection towards the coast of low-level flows heavily laden with moisture during the autumn period (Ricard et al., 2012). This article aims to analyse the statistical coherence between the WVMR Level–2 products derived from IASI on board METOP-C and the Raman lidars involved during WaLiNeAs. It includes complementary analyses with ERA5 which uses IASI radiances in its assimilation scheme.

Section 2 describes the various Raman lidars used and the ground-based stations, while Section 3 gives an overview of IASI and ERA5. The method used to compare the lidar data with the IASI and ERA5 operational products is presented in Section 4. Section 5 presents and discusses the statistical results. The conclusion is given in Section 6.

2 WaLiNeAs field experiment

2.1 Site and lidar descriptions

The comparison between the WVMR ground-based lidar measurements and the IASI operational products took place in the frame of WaLiNeAs between October 2022 and January 2023. The WVMR vertical profiles derived from the IASI spaceborne spectrometer were compared with those measured by eight Raman lidars located along the western Mediterranean coast of Europe as shown in Figure 1. Table 1 shows the geographical location of each site and their identification number used throughout the article. The main characteristics of the eight Raman lidars are summarised in the Appendix A alongside the calibration process for each Raman lidar.

The technology used for each lidar is similar, as is the data inversion procedure. Useful references are given in Table 1. The maximum uncertainty lies with the contributions of bias and standard deviation. The bias is mainly due to the lidar calibration, aerosol correction and temperature dependency of the backscatter cross section of the H_2O Raman channel (Whiteman, 2003), whereas the standard deviation is due to shot noise. For this study, we will only consider measurements with a statistical error of less than 0.4 g kg^{-1}. In the majority of cases, biases remain less than 5%. As explained in Appendix B, they are strongly dependent on Raman lidar technology. Note that the Raman lidar of Barcelona and Ajaccio use a rotational channel on dinitrogen and dioxygen (N_2+O_2) whereas the others lidar use a roto–vibrational channel on N_2.

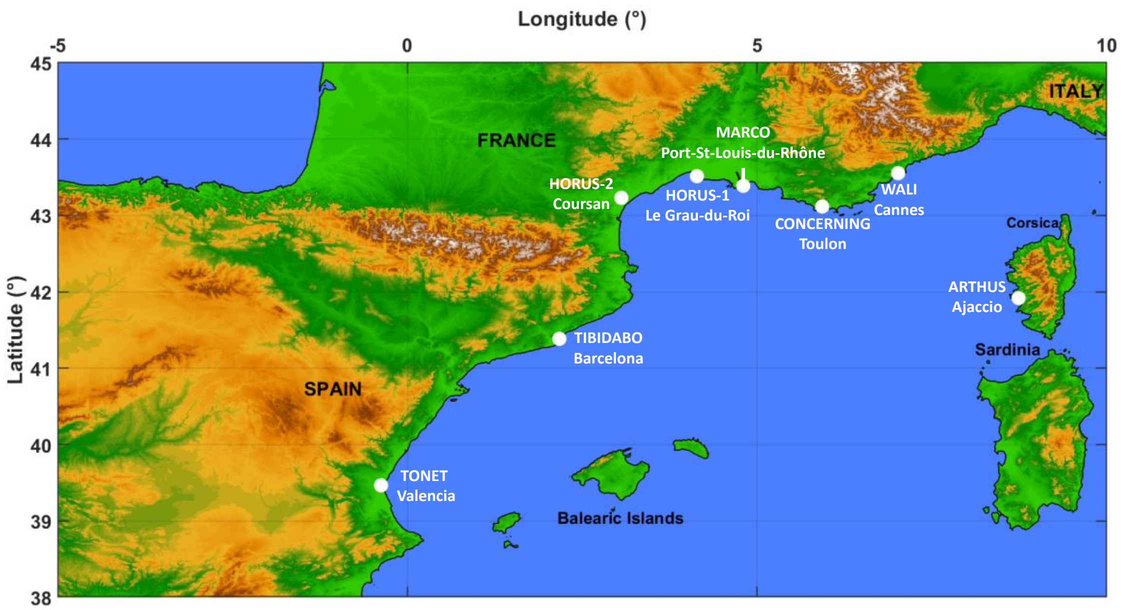

Figure 1: Location of the eight stations (in white) of the Raman lidar network deployed during the WALINEAS field campaign.

Table 1: Raman lidars (RL) involved during WaLiNeAs, their locations and identifications (Id) during the project.

Raman lidar	**Close location**	**Longitude east / Latitude north Altitude amsl**	**Id**
TONET (ACTRIS) (New lidar)	Valencia	-0.42° / 39.5° 60 m	RL1
TIBIDABO (ACTRIS) (Kumar et al., 2011)	Barcelona	2.11° / 41.38° 115 m	RL2
HORUS-2 (Laly et al., 2024)	Coursan	3.06° / 43.23° 4 m	RL3
HORUS-1 (Laly et al., 2024)	Grau-du-Roi	4.13° / 43.52° 7 m	RL4
MARCO (Di Girolamo et al., 2023b)	Port-Saint-Louis-du-Rhône	4.81° / 43.39° 5 m	RL5
CONCERNING (Di Girolamo et al., 2023a)	Toulon	6.01° / 43.14° 65 m	RL6

WALI (Chazette et al., 2014b)	Cannes	6.96° / 43.54° 4 m	RL7
ARTHUS (Lange et al., 2019)	Ajaccio	8.85°/41.70° 20 m	RL8

2.2 Spaceborne and modelling data

2.2.1 MetOp/IASI

IASI is a Fourier transform spectrometer on board a series of three polar heliosynchronous orbiting satellites, which were launched in 2006, 2012 and 2018, respectively. It is part of the MetOp program, which forms the space segment of the overall EUMETSAT Polar System (EPS) (Klaes et al., 2007). The orbit has a 29-day cycle, and the ground track crosses the equator at 09:30 local time. IASI operates in the spectral region between 645 and 2,760 cm^{-1}, achieving a resolution of 0.5 cm^{-1} after apodisation. Its ground swath width is approximately 2,200 km, providing global Earth coverage twice per day. The main objective of the spaceborne mission is to provide global-scale constraints for operational meteorology (Coopmann et al., 2020), with a second mission focused on atmospheric composition (Clerbaux et al., 1998; Cuesta et al., 2020). IASI makes a significant observational contribution to variational assimilation for weather forecasting (Hilton et al., 2009; Guidard et al., 2011). Although radiances are assimilated directly, analysis and reanalysis datasets are only generated using channels with weight functions selected above 2 km amsl, the planetary boundary layer (PBL) is therefore less directly constrained by IASI measurements.

The IASI Level-2 processing development specifically aimed to generate operational WVMR profiles (available at https://data.eumetsat.int/data/map/EO:EUM:DAT:METOP:IASSND02#, last access: 20 December 2025), which are currently distributed on a 90-level grid extending between 0.005 and 1050 hPa (August et al., 2012; Schlüssel et al., 2005). The products are derived from the release 1.1 of the climate data record of "all-sky" temperature and humidity profiles and their associated quality parameters using the latest operational EUMETSAT algorithms available (V6.5.4, 12/2019) (EUMETSAT, 2022). IASI-derived WVMRs are obtained under cloud-free conditions, with vertical resolution of 1–2 km in the lower troposphere (Hilton et al., 2012a) and horizontal resolution of 25 km x 25 km. Nevertheless, operational products are provided at around 40 levels between sea level and 5 km amsl, for vertical sampling ranging from 20 m near the surface to 250 m at 5 km amsl. To compare with lidar data, the WVMR profiles derived from IASI were then linearly interpolated to match the vertical resolution of the lidars of 100 m. Note that for the WVMR retrieval, the IASI weighting functions generally reach a maximum value above 700 hPa. Consequently, sensitivity to the lower troposphere is reduced, leading to greater error below 3 km, where ~80% of moisture is present. The mean relative uncertainty of the WVMR product is given to be 10%.

2.2.2 ERA5

The WVMR profiles derived from the European Centre for Medium-Range Weather Forecasts (ECMWF) Reanalysis (ERA5) (Hersbach et al., 2020) are used for pressure level above 500 hPa (https://cds.climate.copernicus.eu/, last access 31 August 2025). They correspond to altitudes below 5 km amsl, which are distributed over 15 levels. The vertical resolution is approximately 200 m near ground level and 700 m at 5 km amsl. The ERA5–derived WVMR are then interpolated to match the vertical resolution of the lidar profiles. The horizontal resolution is 0.25° of longitude by 0.25° of latitude, which is approximately equivalent to 21 km by 28 km at a latitude of 40°.

2.3 Meteorological context

Autumn 2022 was characterised by unusual weather conditions in the western Mediterranean basin, including persistent positive temperature anomalies and widespread rainfall deficits. This followed an exceptionally hot summer, the effects of which continued into autumn through enhanced atmosphere-ocean interactions. Indeed, temperatures were well above normal levels (~3°C), particularly in September and October. Significant positive temperature anomalies were observed over southern Europe and the western Mediterranean, reflecting the persistence of warm air masses and atmospheric blocking patterns. These conditions were reinforced by exceptionally high sea surface temperatures of the western Mediterranean Sea, resulting from heat accumulation during the summer of 2022. Compared to climatology, anomalies of several degrees (~4°C) were observed (Guinaldo et al., 2023).

Despite this thermodynamic context being favourable to instability, atmospheric circulation on a synoptic scale was dominated by recurrent anticyclonic conditions over Western Europe and the Mediterranean basin. This limited the intrusion of low-pressure systems and the establishment of unstable southerly flows, reducing the frequency and intensity of the Mediterranean weather systems typically observed in autumn (Blanchet et al., 2021). Consequently, autumn total precipitation amounts were significantly below normal by ~24%.

Despite the lower troposphere being drier than normal, two contrasting periods were observed. These periods are evident in the temporal syntheses derived from IASI measurements, as illustrated in Figure 2, which depicts the precipitable water content over the western Mediterranean basin. Figure 2a shows the wettest period, while Figure 2b shows the driest period after 5 November 2022. The temporal evolution of lidar, spaceborne and modelling data in the supplementary material will highlight this. Precipitable water content is homogeneous across the western basin, but there is a significant variation between the two periods, with a ~30% decrease between the beginning of November and the rest of the year.

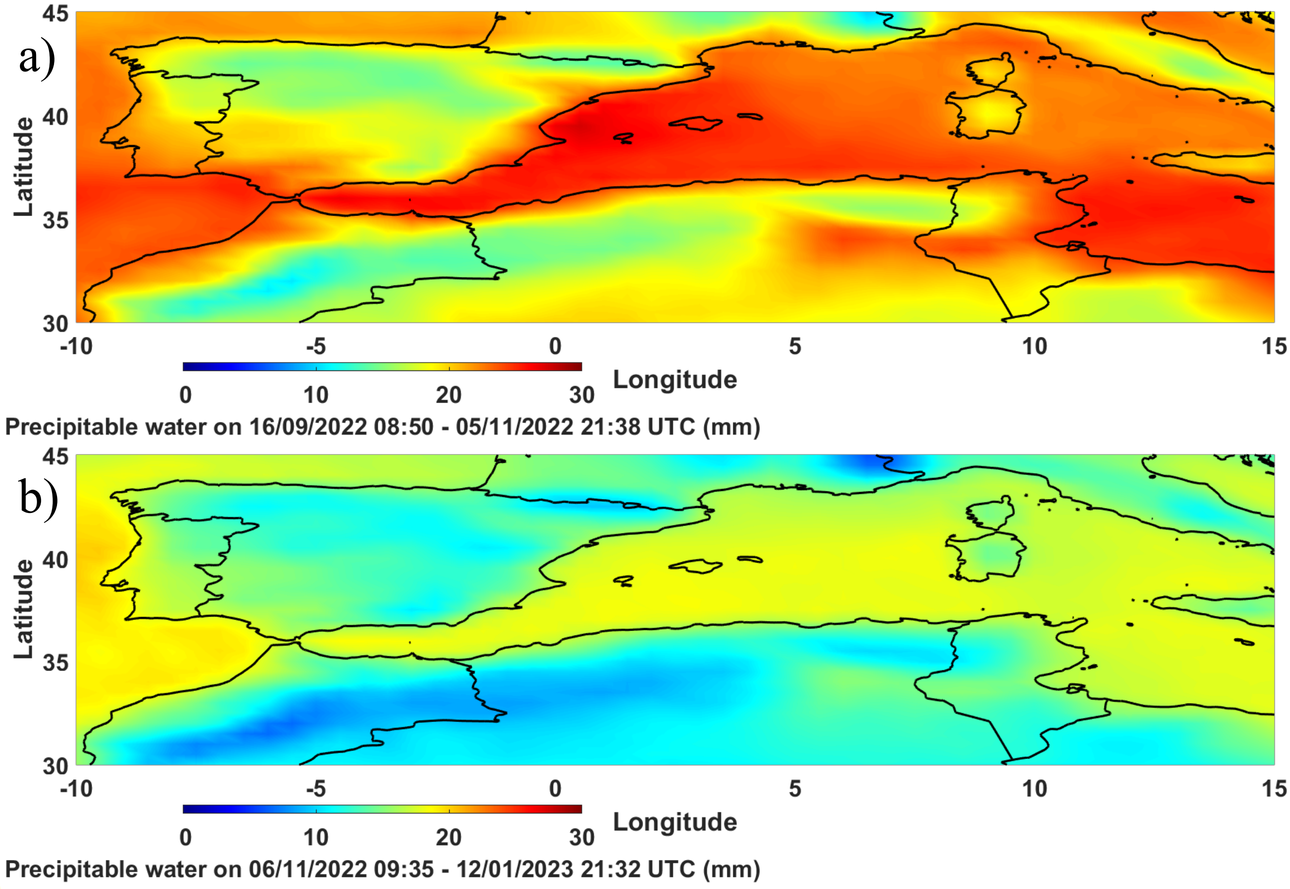

Figure 2: Precipitable water derived from IASI products during the wet period (16 September to 5 November 2022) and the dry period (6 November 2022 to 12 January 2023), as observed during the WaLiNeAs field campaign.

3 Data processing methods

3.1 Consistency between lidar calibrations

The lidars were calibrated individually using radiosondes and/or ground-based weather stations using similar approaches. This raises the question of how to standardize these different calibration procedures. To assess this, we compared each lidar's data over its entire operating period with reanalyses of ERA5. ERA5 is constrained by multiple sources of vertical profiles, including radiosondes, the IAGOS (In-Service Aircraft for a Global Observing System) network and IASI observations above 2–3 km (Hersbach et al., 2020). For this reason, ERA5 most closely mimics the hourly radiosonde observations that would have been available near the various lidar stations of the WaLiNeAs network. As an example, we present the comparison between all radiosondes and ERA5 for the period November–December 2022 at the meteorological station of Nîmes (Météo-France), located 40 km north of Grau-du-Roi, in the supplementary material (Figure S1). The relationship is linear with a slope of 0.99 and an intercept of 0.054 g kg^{-1}, a strong correlation of 0.99 and a low mean bias of +0.02 g kg^{-1}. The standard deviation is around 0.36 g kg^{-1}. Furthermore, as shown in Laly and Chazette (2025), for the sites of the Grau-du-Roi (RL4) and Cannes (RL7), the ERA5 pixels around a central pixel are strongly correlated (COR > 0.97), and exhibit MBs with an absolute value below 0.14 g kg^{-1}.

For all lidars, we therefore sought a calibration yielding a slope of 1 in the comparison with ERA5. This required applying a site-specific correction factor. As shown in Table 2, the correction factors range from 0.93 to 1.1 with values mostly close to 1. This attests to the quality of the original calibrations carried out independently at each station. More or less significant biases between lidar and ERA5 remain, as shown in the Supplementary Figures S2 to S9. In some cases, these may be associated with imperfect calculation for molecular and particulate contributions in the lidar data. Nevertheless, the same process has been used to correct all lidar signals for molecular transmission, and the residual error is below 0.02 g kg^{-1}. The contribution of aerosols remains small, either because aerosol optical thickness (AOTs) values are mainly below 0.1, or because the aerosols are primarily desert dust with Ångström exponents below 0.5 (Appendix B). Note that RL2 and RL8 use a rotational Raman channel for oxygen and nitrogen in addition to the vibro-rotational Raman channel for water vapour. Because the wavelength difference is larger in this configuration, the effect of aerosols is more pronounced. Failure to correct for aerosols leads to an overestimation of the WVMR. As shown in Appendix B, for a typical AOT of 0.1 (at 355 nm) and an Ångström exponent of 1.5 (corresponding to pollution aerosols), the overestimation could reach approximately +1% for the use of N_2–channel and +2% for the use of N_2+O_2–channel, and decreases progressively with decreasing distance to the lidar. It is less than +1% (between +1.3% and +5%) for dust aerosol mixed and above the marine boundary layer for the altitudes lower than 1.5 km a.m.s.l. (above 1.5 km a.m.s.l.).

Another potential source of bias is imperfect correction of the overlap factor in the lower layers. The minimum range of WVMR data is ensured to be below 200 m (see Table 1) because the N_2– and H_2O–Raman channels share the same optical path. The remaining divergences are mainly related to the near range due to the angular acceptance of the interference filters. Overall, biases related to the instrument itself and to the data inversion procedure remain below or on the order of 0.1 g kg^{-1} for all lidars. This justifies performing only a slope correction with respect to ERA5, given the good coefficients of determination obtained (between 0.71 and 0.91).

The intercept values reported in Table 2, representing systematic biases, are the result of multiple contributions that can partially cancel each other. Nevertheless, biases with an absolute value greater than 0.1 g kg^{-1} are considered more likely attributable to modelling rather than instrument error. For this reason, such intercepts in Table 2 have not been used in the lidar calibration process.

Table 2: Statistical parameters of the regression between lidar and ERA5 data. The calibration correction factor must be applied to each lidar data set in order to obtain a slope of 1 for the regression line.

	RL1	RL2	RL3	RL4	RL5	RL6	RL7	RL8
Calibration correction factor	1.10	1.02	1	1.01	1.06	0.93	0.99	1
Intercept	0.03	0.54	0.67	1.00	0.62	0.10	0.45	0.19

($g\ kg^{-1}$)								
Coefficient of determination	0.88	0.83	0.91	0.87	0.75	0.82	0.91	0.87

3.2 Statistical metrics

Comparisons between LIDAR measurements and IASI overpasses were performed by considering the nine pixels surrounding each site (Figure 3), corresponding to an area of 75 km x 75 km. Due to variations in horizontal wind speed, the nine pixels do not provide the same level of representation at different altitudes. During the period under consideration, wind speeds were below 20 m s^{-1}, ensuring that observations above the sites were accurately captured by at least one of the pixels. Furthermore, variability in vertical humidity profiles across these IASI pixels was low, averaging less than 0.2 g kg^{-1}. Additionally, as the stations are situated close to the coast, at least four of these pixels consistently provide data on the lower troposphere. The lidar data were averaged over a one-hour period, using profiles within ±30 minutes of the satellite overpass time. The signal-to-noise ratio is significantly improved by this averaging, with uncertainties of less than 0.4 g kg^{-1} being achieved in the low troposphere. The number of IASI pixels contributing to the comparison varies with altitude, as the surrounding topography must be taken into account. Within the perimeter defined by the nine pixels, the local summits generally remain below 500 m amsl, ensuring minimal topographic effects in the low troposphere including the PBL.

The statistical indicators used to evaluate the consistency of the IASI-derived WVMR (r_{iasi}) with respect to lidar measurements (r_{lidar}) are the mean bias (MB), the root mean square difference (RMSD), the root mean square error (RMSE) and the (Pearson) correlation (COR). These metrics are commonly used to assess model performance (Boylan and Russell, 2006; Tombette et al., 2008) and given for each altitude z by:

$$MB(z) = \langle r_{lidar}(\mathrm{t,z}) \rangle - \langle r_{iasi}(\mathrm{t,z}) \rangle \quad (1)$$

$$RMSD(z) = \sqrt{\langle (r_{lidar}(\mathrm{t,z}) - r_{iasi}(\mathrm{t,z}))^2 \rangle} \quad (2)$$

$$RMSE(z) = \sqrt{RMSD(z)^2 - MB(z)^2} \quad (3)$$

$$COR(z) = \frac{\langle (r_{lidar}(\mathrm{t,z}) - \langle r_{lidar}(\mathrm{t,z}) \rangle) \cdot (r_{iasi}(\mathrm{t,z}) - \langle r_{iasi}(\mathrm{t,z}) \rangle) \rangle}{\sqrt{\langle (r_{lidar}(\mathrm{t,z}) - \langle r_{lidar}(\mathrm{t,z}) \rangle)^2 \rangle \cdot \langle (r_{iasi}(\mathrm{t,z}) - \langle r_{iasi}(\mathrm{t,z}) \rangle)^2 \rangle}} \quad (4)$$

where ⟨ ⟩ is the temporal averaging. The altitude averaged MB ($\widetilde{MB}$) and RMSE ($\widetilde{RMSE}$) are then derived using the relationships:

$$\widetilde{MB} = \frac{1}{M} \cdot \sum_{i=1}^{M} MB_i(z)$$
$$\widetilde{RMSE} = \sqrt{\frac{1}{M} \cdot \sum_{i=1}^{M} RMSD_i(z)^2 - \widetilde{MB}^2} \quad (5)$$

were M is the number of lidar samplings i along the altitude.

The CORs from different altitudes are combined using the Fisher $\mathcal{F}$ transformation (Fouladi and Steiger, 2008). This gives the following equation for each altitude z:

$$\mathcal{F}(z) = \frac{1}{2} \cdot \log\left(\frac{1 + COR(z)}{1 - COR(z)}\right) \quad (6)$$

which leads to the COR averaged on the altitudes ($\widetilde{COR}$) expressed by:

$$\widetilde{COR} = \frac{e^{2\cdot\bar{\mathcal{F}}} - 1}{e^{2\cdot\bar{\mathcal{F}}} + 1} \quad (7)$$

with $\bar{\mathcal{F}} = \int_{z_a}^{z_b}(N(z) - 3)\cdot\mathcal{F}(z)\cdot dz \Big/ \int_{z_a}^{z_b}(N(z) - 3)\cdot dz$,

where *N(z)* represents the number of coincidences between Raman lidar and IASI at altitude *z*. *N(z)*-3 is an approximation used when the number of samples is less than or around 50 (Stuart and Ord, 1991). Note that the same approach is applied when lidar and ERA5 are compared.

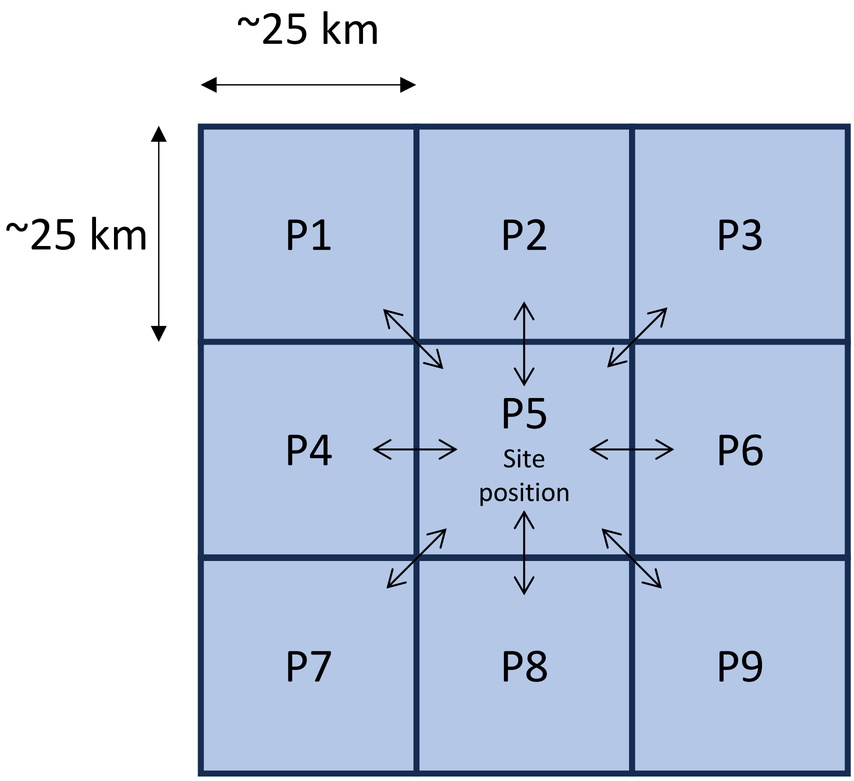

Figure 3: IASI pixels selected for comparison with lidar measurements. The central pixel includes the location of the lidar site. The horizontal resolution is 25 km x 25 km for the water vapour product.

4 Results

The temporal evolution of the WVMR vertical profiles corresponding to lidar measurements and coincident IASI overpasses is presented in the supplementary material. (Figures S10 to S17). Profiles derived from ERA5 are also provided. As the lidars did not operate during the same periods, the temporal dynamics differ among stations. The wettest period occurs before 5 November 2022, after which the dry period begins. This transition takes place slightly later in Corsica due to the island's susceptibility to southerly winds from North Africa. The presence of clouds limits the range of lidar systems and increases measurement dispersion. They can be identified on the lidar profiles, and only the data beneath the clouds is considered. The low clouds can be easily identified in the figures by the altitude range of the lidar measurements. However, there was much less precipitation than average for this region, with only one 100 mm daily precipitation event observed in Corsica around 13 November 2022. Hence, the number of coincidences with IASI varies as a function of altitude, as shown by the vertical profiles of MB, RMSE and COR presented in the supplement (Figures S18 to S25). The number of samples decreases as altitude increases. This is due to the limited range of Raman lidars during daytime and under thick cloud cover.

4.1 Statistical results

Table 3 summarises the statistical analysis for: i) the PBL (0.2–1.5 km amsl), ii) the transition layer to the free troposphere (1.5–3 km amsl), iii) the free troposphere (3–5 km amsl), and iv) all three layers combined. It is worth noting that the altitude of the top of the PBL varies over time. The first two layers in Table 3 may therefore include air-mass recirculation associated with the sea-land breeze cycle and circulation patterns that are very specific to the measurement site.

A synthesis of the behaviour of all lidar systems has been obtained by combining statistical profiles obtained from individual lidar systems (Figure 4). The resulting synthesis across all lidar stations shows that the vertical profiles of the three statistical parameters exhibit relatively smooth continuity between adjacent layers, highlighting that the variability of the PBL height has on average a moderate influence. This is more noticeable at sites expose to strong winds, such as the Rhône delta and Barcelona. At these sites, a decrease in correlation is observed at the interface between the PBL and the free troposphere.

In general, there is a significant correlation between lidar and IASI measurements, mainly ranging from 0.7 to 0.8 (Figure 4a). This strong correlation is also evident between lidar measurements and ERA5 reanalyses. However, at the Barcelona (RL2) and Coursan (RL3) sites weaker correlations are observed (between ~0.5 and 0.7). For Coursan, the reduced correlations are less significant, given the much lower number of coincidences and the reduced range of the lidar, mainly due to frequent cloud cover. The slightly lower correlations values determined for Barcelona (RL2) can be possibly explained by the location of this lidar station. It is located in an urban environment at the foothill of a 500-meter-high mountain range, and 5 kilometres from the sea. Pérez et al. (2004) have shown that, in such conditions, the atmospheric vertical structures are complex, making comparisons with reference profiles (e.g., radiosondes) problematic. In most cases, the correlations between lidar and ERA5 are slightly higher than those between lidars and IASI for all layers. This may be attributed both to the assimilation of additional observational datasets in ERA5, beyond IASI, and to the lower sensitivity of IASI within the PBL. Nevertheless, WVMR profiles derived from IASI properly represent atmospheric variability occurring from one satellite overpass to another.

The RMSEs values are fairly consistent when comparing the different lidars and remain mostly between 1 and 2 g kg^{-1}, regardless of the layer considered (Table 3). It should be remembered that only lidar data with a statistical error of less than 0.4 g kg^{-1} were considered in this study. The RMSEs shown in both Table 3 and Figure 4b are significantly higher and reflect the statistical variability between the lidar and IASI or ERA5 data. These values provide a clear indication of the uncertainty in the vertical WVMR profiles derived from IASI or ERA5 in the first 5 km of the atmosphere, where most of the water vapour is present. Note that differences between the single lidar and IASI or ERA5 profiles reverberate more on RMSE, which make use of absolute differences (root-mean square), than on bias, which accounts for the sign of the differences, most part of those cancelling out. One possible source of the high RMSE values may be the displacement of air masses between IASI or ERA5 pixels, resulting in spatial heterogeneity between pixels.

Interpreting biases is more difficult because of their diverse origins, which are not always identifiable. As explained in Appendices A and B, biases related to lidar measurements are mainly associated with i) the reference used for calibration, ii) the differential transmission due to aerosols, and iii) the temperature dependence of the Raman backscatter cross section (Appendix B). The lidars were individually calibrated using in situ measurements (e.g. weather stations or radiosondes) and subsequently recalibrated by adjusting the calibration slope using coincident ERA5 data for each site (see Section 3.1). The biases relative to IASI and ERA5 are presented in Table 3 after accounting for the biases related to temperature and aerosols affecting the lidar products. The corresponding vertical profiles are provided in the supplementary material (Figures S18b to S25b) and in Figure 4b; however, the contributions of aerosols and temperature to the bias are not considered in these figures.

In the synthesis, the bias values relative to IASI are higher than those relative to ERA5 for all altitude ranges. The difference ranges from 0.19 to 0.26 g kg^{-1}. For the individual sites, the vast majority of biases (lidar–IASI or lidar–ERA5) are positive, indicating a systematic underestimation of the water vapour content by IASI and to a lesser extent by ERA5.

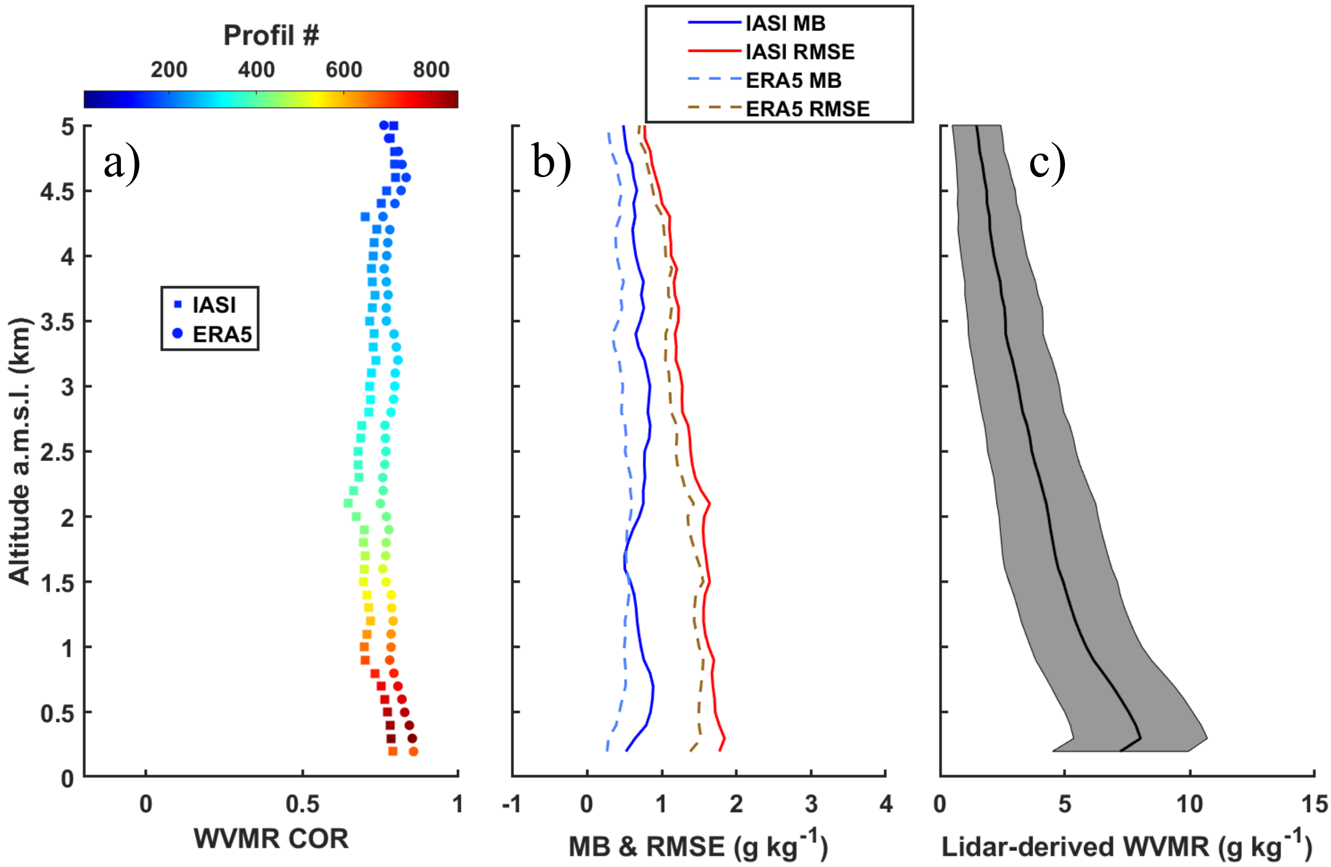

Figure 4: Synthesis of the statistical coefficients across all lidar stations when comparing lidar measurements with IASI and ERA5 products. the vertical profiles show a) the correlation coefficient (COR); b) the mean bias (MB, lidar - IASI and lidar - ERA5) and the root mean square error (RMSE); c) the mean water vapour mixing ratio (WVMR) profile of all the overpasses of IASI. The synthesis profiles have been obtained by combining statistical profiles derived from individual lidar systems. The contributions of aerosols and temperature to the bias are not considered.

Table 3: Statistical results (mean bias MB, root mean square error RMSE and correlation COR) synthesized from the comparisons between lidar measurements and i) IASI measurements (Bold) and ii) ERA5 reanalysis (Italic). Plain text denotes instances where the statistic is considered not representative due to insufficient data or range limitations. The number of samples for each site is shown in the supplementary material (see Figures S18 to S25). The biases related to temperature and aerosols have been subtracted. The synthesis was carried out by weighting each site according to its number of measurements.

Altitude range (km amsl)	RL1	RL2	RL3	RL4	RL5	RL6	RL7	RL8	All
MB (lidar-IASI or *ERA5*) (g kg^{-1})									
[0.2 5]	-	**+0.59** ***+0.16***	+1.30 *+0.73*	+1.40 *+1.27*	+0.70 *+0.49*	**+0.07** ***-0.12***	**+0.63** ***+0.40***	**+0.22** ***+0.01***	**+0.54** ***+0.31***
]0.2 1.5]	**+0.72** ***+0.11***	**+0.80** ***+0.16***	**+1.33** ***+0.59***	**+0.92** ***+0.93***	**+0.57** ***+0.39***	**+0.29** ***+0.05***	**+0.42** ***+0.33***	**+0.36** ***-0.02***	**+0.51** ***+0.26***
]1.5 3]	-	**+0.49** ***+0.12***	+1.24 *+0.84*	**+1.28** ***+1.14***	**+1.16** ***+0.94***	**+0.06** ***-0.10***	**+0.69** ***+0.37***	**+0.14** ***+0.09***	**+0.54** ***+0.35***
]3 5]	-	**+0.54** ***+0.18***	+1.33 *+0.73*	+1.80 *+1.61*	+0.44 *+0.23*	**-0.05** ***-0.25***	**+0.74** ***+0.47***	**+0.19** ***-0.03***	**+0.56** ***+0.30***
RMSE (g kg^{-1})									
[0.2 5]	-	**1.58** ***1.47***	1.53 *1.38*	1.36 *1.02*	1.64 *1.43*	**1.28** ***1.24***	**1.13** ***0.97***	**1.25** ***1.12***	**1.39** ***1.25***
]0.2 1.5]	**1.72** ***1.26***	**1.95** ***1.78***	**1.71** ***1.74***	**1.52** ***1.02***	**1.90** ***1.53***	**1.67** ***1.67***	**1.35** ***1.10***	**1.66** ***1.55***	**1.68** ***1.49***
]1.5 3]		**1.79** ***1.83***	1.56 *1.34*	**1.42** ***1.01***	**1.54** ***1.38***	**1.27** ***1.14***	**1.20** ***1.06***	**1.36** ***1.20***	**1.47** ***1.29***
]3 5]	-	**1.02**	1.37	0.97	1.36	**0.92**	**0.88**	**0.72**	**1.08**

		0.79	*1.11*	*0.90*	*1.28*	***0.92***	***0.79***	***0.60***	***0.99***
COR									
[0.2 5]	-	**0.62** ***0.69***	0.55 *0.64*	0.78 *0.89*	0.66 *0.77*	**0.72** ***0.73***	**0.82** ***0.86***	**0.73** ***0.79***	**0.73** ***0.80***
]0.2 1.5]	**0.64** ***0.82***	**0.69** ***0.76***	**0.52** ***0.63***	**0.82** ***0.92***	**0.69** ***0.81***	**0.76** ***0.76***	**0.82** ***0.87***	**0.70** ***0.76***	**0.74** ***0.81***
]1.5 3]	-	**0.52** ***0.49***	0.48 *0.57*	**0.70** ***0.87***	**0.67** ***0.76***	**0.72** ***0.75***	**0.79** ***0.84***	**0.68** ***0.76***	**0.69** ***0.77***
]3 5]	-	**0.58** ***0.73***	0.67 *0.74*	0.79 *0.83*	0.57 *0.66*	**0.61** ***0.59***	**0.84** ***0.85***	**0.81** ***0.87***	**0.74** ***0.79***

4.2 Discussion

Few comparative studies in the literature exist between IASI and lidar measurements, and the same is true for comparisons between ERA5 reanalyses and lidar measurements. Following the ChArMEx and HyMeX programmes, Chazette et al. (2014a) compared WVMR measurements derived from the WALI lidar, which was located in the Balearic island of Menorca (Spain), with IASI measurements following nighttime overpasses by METOP-A. The RMSE calculated for September–October 2012 was ~1.06 g kg^{-1} between 0 and 5 km amsl, which is consistent with the results presented in Table 3. The MB was around 0.5 g kg^{-1}, slightly higher than the value found in this study, while the COR (~0.66) was also lower. A key difference lies in the fact that the lidar measurements from Menorca were acquired over open sea and included heavy precipitation events (HPEs), whereas the WaLiNeAs measurements were taken at coastal sites and were not affected by HPEs. A mutual bias value of 0.26 g kg^{-1} was reported by De Rosa et al. (2020) when comparing the Raman lidar BASIL and IASI in the altitude interval 2-15 km (RMSE = 0.30 g kg^{-1}). More recently, Laly and Chazette (2025) investigated the potential impact of atmospheric water vapour Raman lidar measurements by comparing them with WVMR vertical profiles obtained from ERA5 data. This work was also carried out as part of the WaLiNeAs project and included the Grau-du-Roi (RL4) and Cannes (RL7) sites during the dry period. In the first 5 kilometres of the atmosphere, they found an RMSE of 1.05 g kg^{-1} for the Cannes (RL7) site, which is comparable to the results in Table 3 (0.97 g kg^{-1}). For this site, the MB also remained fairly similar, with a minimal value of ~+0.4 g kg^{-1} compared to +0.25 g kg^{-1} after accounting for aerosol and temperature contributions. The COR correlations are also similar (0.89 compared to 0.86). At the Grau-du-Roi site (RL4), the RMSE was slightly higher, at 1.57 g kg^{-1} compared to 1.02 g kg^{-1} in this study. However, the MB and COR were comparable, with values being higher and on the order of +1 g kg^{-1} and 0.86, respectively.

Based on the study presented here, larger dispersion of results might have been expected for the two stations (RL4 and RL5) located in the Rhône Valley. In the Rhône Valley, there is often a process of recirculation, whereby the Mistral wind blows in altitude and the sea breeze blows lower down. The latter can penetrate more than 100 km inland. In addition, the lower layers in the Camargue can be very humid due to the abundance of liquid water areas. There is also a steep humidity gradient between the Mediterranean coast and inland areas, associated with various local phenomena linked to the Rhône delta's specific topography. The statistical results presented here show that the temporal variability of WVMR over the first five kilometres is accurately represented by both IASI measurements and ERA5 reanalyses.

As previously explained, during the WaLiNeAs field campaign, there was a wetter period in October, followed by an exceptionally dry period from early November onwards. Most of the measurements were taken during the drier period. The wetter period was less sampled, except in Barcelona (RL2), Toulon (RL6) and Ajaccio (RL8). At the Barcelona station (Figure S11), more than two-thirds of the measurements were taken during the wetter period, which may be subjected to greater variability than the drier period. This may also explain the slightly weaker correlations observed for this station (Table 3 and

Figure S19a) in addition to its specific location. Note that it is more difficult to draw conclusions about the samples in the free troposphere, as there are fewer of them during the wetter period when there was heavy cloud cover.

A synthesis was therefore carried out between the Toulon and Ajaccio sites in order to potentially highlight the differences between the wet and dry periods. The results are presented in Figure 5 and Table 4: . During the wet period, there was approximately 30% more water vapour in the lower troposphere. The statistical parameters are comparable for both periods, with an overall IASI bias of 0.25 g kg^{-1} (0.18 g kg^{-1}) for the wet (dry) period. In the case of ERA5, this bias is very small ($\lesssim$ 0.02 g kg^{-1}). The RMSE values remain significantly high, exceeding 1 g kg^{-1}, while the COR values (~0.7) indicate a satisfactory representation of the temporal variability of the WVMR vertical profiles for both the wet and dry periods.

It is interesting to note that METOP/IASI overpasses the western Mediterranean twice a day, at 08:00–10:00 and 19:00–21:00 local time. The second time slot corresponds to early nighttime conditions during the field campaign period. However, it is still early enough in the night for the PBL height to change significantly, particularly near the coast. Therefore, no notable differences were observed between the two time slots, apart from a decrease in samples and statistical representativeness when the two slots are split.

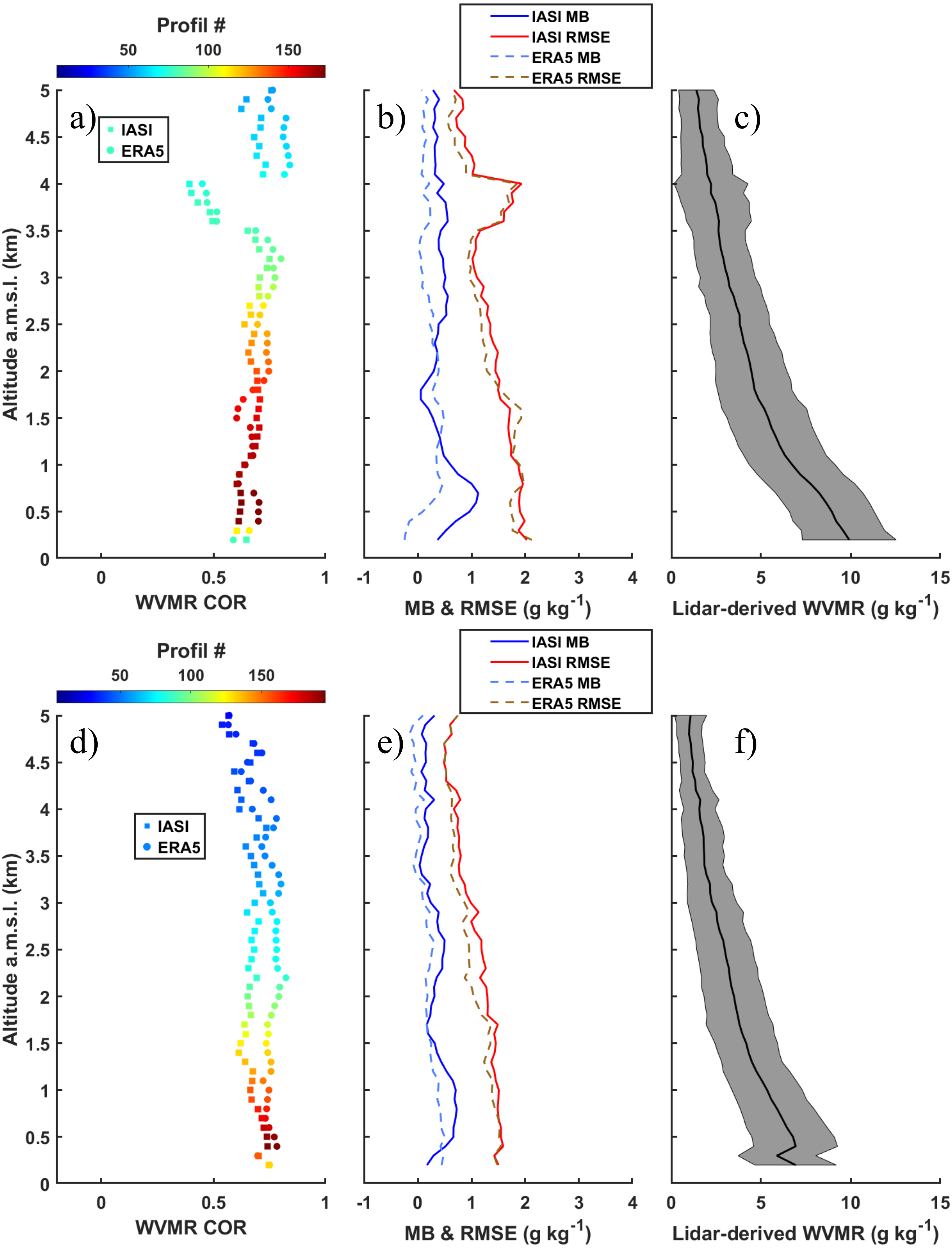

340 **Figure 5 : Synthesis of the statistical coefficients for the Toulon and Ajaccio lidar stations (RL6 and RL8) when comparing lidar measurements with IASI and ERA5 products. Wet conditions are illustrated in panels a)–c), while dry conditions are shown in panels d)–f). The vertical profiles show: a) and d) the correlation coefficient (COR); b) and e) the mean bias (MB, lidar - IASI and lidar - ERA5) and the root mean square error (RMSE); c) and f) the mean water vapour mixing ratio (WVMR) profile of all the overpasses of IASI. The contributions of aerosols and temperature to the bias are not considered.**

Table 4: Statistical results (mean bias MB, root mean square error RMSE and correlation COR) synthesized from the comparisons between lidar measurements and i) IASI measurements (Bold) and ii) ERA5 reanalysis (Italic) for RL6 and RL8. The number of samples for each site is shown in Figure 5. The biases related to temperature and aerosols have been subtracted. The synthesis was carried out by weighting each site according to its number of measurements.

Altitude range (km amsl)	**[0.2 5]**	**]0.2 1.5]**	**]1.5 3]**	**]3 5]**
Wet period				
MB	**+0.25** *+0.01*	**+0.37** *-0.04*	**+0.12** *+0.06*	**0.27** *-0.01*
RMSE	**1.49** *1.42*	**1.87** *1.86*	**1.41** *1.32*	**1.20** *1.10*
COR	**0.66** *0.70*	**0.65** *0.66*	**0.68** *0.72*	**0.65** *0.73*
Dry period				
MB	**+0.18** *+0.02*	**+0.34** *+0.18*	**+0.18** *+0.03*	**+0.07** *-0.10*
RMSE	**1.15** *1.04*	**1.49** *1.42*	**1.23** *1.03*	**0.71** *0.63*
COR	**0.68** *0.75*	**0.69** *0.75*	**0.67** *0.78*	**0.66** *0.72*

5 Conclusion

During the WaLiNeAs field campaign, eight lidar stations, evenly distributed along the Spanish and French coasts of the western Mediterranean, collected a unique set of vertical water-vapour profiles. This dataset, acquired during the exceptionally dry autumn and winter of 2022-2023, aims to assess the value of lidar measurements in the data assimilation process for weather forecasting models. For this purpose, the lidar data were compared with one of the main observational constraints of meteorological models: the European IASI instrument carried on board the METOP satellite series. For completeness, comparisons were also performed with the ERA5 reanalyses provided by ECMWF, which assimilate IASI radiances in the free troposphere.

Lidar measurements mainly provide valuable information in the lower troposphere, which is poorly sampled by IASI, particularly below 3 km. Nevertheless, we show that IASI observations correlate well with the lidar measurements from the WaLiNeAs stations, with correlation coefficients generally exceeding 0.7 within the first 5 km of the atmosphere. The RMSEs quantifying the deviation between lidar and IASI measurements are relatively high, ranging from 1 to 2 g kg^{-1}, whereas the standard deviation of the considered lidar measurements considered is less than 0.4 g kg^{-1}. A systematic underestimation of the WVMR profiles derived from IASI is also observed at all stations, with an average bias of about +0.4 g kg^{-1}. A similar but smaller underestimation is found in ERA5, typically +0.2 g kg^{-1}. This study provided an opportunity to demonstrate the high degree of consistency between the various research lidars, despite having been developed independently by different teams from four countries in Europe. It also demonstrates that lidar measurements can provide additional relevant information for weather forecasting.

The IASI-NG instrument, launched on 12 August 2025, offers 30% more data on water vapour profiles with an improvement in spectral resolution compared with the version used in our study (0.25 cm^{-1} for 0.5 cm^{-1}, https://user.eumetsat.int/resources/user-guides/metop-sg-iasi-ng-l1c-and-l1d-data-guide, last access 26 November 2025). This increase in spectral resolution is accompanied by an increase in vertical resolution. IASI-NG measurements should therefore enable a more accurate characterization of water vapour in the low troposphere. Using a similar lidar framework as in WaLiNeAs would be of particular interest, as lidars appear to provide both a relevant validation tool and a valuable complement to spaceborne measurements.

Appendix A: Lidar descriptions

This appendix outlines the key features of Raman lidars and sites. Table A1 summarises the main lidar characteristics.

Table A1: Characteristics of the water vapor Raman lidar used during the WaLiNeAs field campaign.

	RL1	RL2	RL3	RL4	RL5	RL6	RL7	RL8
Emitted wavelength (nm)	~354.7							
Reception channels (nm)	387.5 407.5	353.9 407.5	387.5 407.5					353.9 407.5
Energy (mJ)	80	90	30	30	0.25	110	100	100
Repetition rate (Hz)	20	20	100	20	20000	100	20	200
Telescope diameter (cm)	30	38	15	15	40	50	15	40
Telescope field-of-view (mrad)	2.1	2	1.6	1.6	0.31	0.55	1.6	0.6
Laser divergence (mrad)	0.7	0.5	0.2	0.2	0.3	0.39	0.2	0.4
Power-aperture product ($W\ m^2$)	0.11	0.20	0.053	0.011	0.63	2.16	0.035	2.5
Native vertical resolution (m)	7.5	3.75	0.75	0.75	15	7.5	0.75	7.5
Final vertical resolution (m)	100							
Maximum daytime range (km)	-	1.5	2	1.5	2	3-4	2	4
Maximum nighttime range (km)	4.5	6	8	7	5	6	10	12
Minimum range of WVMR data (m)	200	90	150	150	100	100	150	200
Native time resolution (min)	1	1	1	1	0.05	0.17	1	0.17
Final time resolution (min)	30							

A.1 TONET at Valencia (RL1)

TONET Lidar is deployed at Burjassot Atmospheric meaSurement Station (BASS, 39.5 ºN, -0.42 W, 60 m amsl). It is an Aerosol Remote Sensing (ARS) site of the Aerosol, Clouds and Trace Gases Research Infrastructure (ACTRIS) located in the metropolitan area of Valencia city, 10 km distant to the Mediterranean Sea. TONET Lidar is 8-channel Raman depolarization Lidar (LR332-D300) manufactured by Raymetrics S.A. The instrument is equipped with a Nd:YAG pulsed laser beam emitting 80 mJ at 355 nm pointed vertically upward. The receiver is based on a 30 cm Cassegrain optical telescope design. Two Raman detection channels were used for the field-campaign: one for nitrogen (386.6 nm) and the other for water vapour (407.5 nm). The backscattered signal is detected using photomultiplier tubes (PMTs) and then by a 16-bit analogue-to-digital (A/D) converter. The sampling is either in analogue and photon-counting modes with a rate of 20 and 800 MHz, respectively, providing 1-minute averaged profiles with vertical resolution of 7.5 m. The full overlap is reached around 250 m for all channels. Due to TONET's configuration, only nighttime measurements were taken during WaLiNeAs campaign. Thus, we have 1-month of available data, around 12 hours per day (6 pm. – 6 am) from 20th October to 20th November. The WVMR measurements has been calibrated using collocated ground-based meteorological measurements (Chazette et al., 2025).

A.2 TIBIDABO at Barcelona (RL2)

TIBIDABO is a multiwavelength Raman lidar operating at the Barcelona Aerosol Remote Sensing site of ACTRIS (https://www.actris.eu/, last access: 28 November 2025). The instrument, which is documented in (Kumar et al., 2011), is installed on the rooftop of the D3 building in the Campus Nord of Universitat Politècnica de Catalunya (UPC), in Barcelona, Spain (41.38° N, 2.11° E; 115 m amsl). This location is in an urban environment, at the bottom of a 500-m altitude mountain range, near the end of the range yielding to the wide Llobregat river valley, at 5 km distance from the sea and 6 km of the Barcelona harbour area. Concerning the water vapor measurements, the system emits 90 mJ at 354.7 nm for a repetition rate of 20 Hz. It uses a 38 cm receiving telescope and detects the returns corresponding to the vibro-rotational Raman scattering of water molecules at 407.5 nm (0.3-nm IF bandwidth), and to the pure-rotational Raman scattering of nitrogen and oxygen at 353.9 nm (0.8-nm IF bandwidth, OD8 at the elastic wavelength and optimized for being temperature independent). Calibrations are performed using daily radiosondes, launched at 500-m distance from the lidar instrument.

A.3 HORUS at Coursan and Grau-du-Roi (RL3 and RL4)

The H_2O Raman Ultraviolet Sounder (HORUS) (Laly et al., 2024) was installed in Coursan (HORUS–2, 43.23° N 3.06° E, 4 m amsl.) and Le Grau-du-Roi (HORUS–1, 43.52° N 4.13° E, 7 m amsl). Coursan is a town surrounded by lowland landscapes. The river Aude flows through it and there are numerous wetlands. A high proportion of the land is used for agriculture. Le Grau-du-Roi is a south-east-facing coastal site located to the west of the Camargue region. It is bordered by a long sandy beach and surrounded by low-lying terrain. It lies in the southern section of the Rhône delta, where numerous wetlands provide ideal conditions for evaporation.

HORUS lidars have been especially developed for the WaLiNeAs field campaign by Climate and Environmental Sciences Laboratory (LSCE) to measure water vapour profiles in the low troposphere in the framework of WaLiNeAs. HORUS is a new generation of compact, autonomous, eye-safe systems that work with pulsed frequency-tripled Nd:YAG lasers manufactured by Lumibird Quantel. The optical architecture of the HORUS lidar is identical to that of the WALI lidar (described in subsection 2.6). The HORUS-1 model has a pulse energy of 30 mJ at a wavelength of 354.7 nm and a pulse repetition frequency (PRF) of 20 Hz. In contrast, the HORUS-2 model has an PRF of 100 Hz.

Calibration was performed using radiosondes prior and after the field campaign and ground-based meteorological measurements (Laly et al., 2024). The statistical uncertainty is less than 0.3 g kg^{-1} for the 1–hour averaged profile below 2 km amsl. with a bias of less than 0.50 g kg^{-1}. The HORUS dataset is available as NetCDF files and can be freely downloaded from the AERIS database (https://doi.org/10.25326/537, last access: 31 August 2025). Each vertical profile of WVMR is associated with a statistical error profile.

A.4 MARCO at Port-Saint-Louis-du-Rhône (RL5)

The Micro-pulse Atmospheric optical Radar for Climate and weather Observations (MARCO, Di Girolamo et al., 2023b) was deployed at Direction des Services Techniques (Port-Saint-Louis-du-Rhône, 43.39° N, 4.81° E, 5 m amsl). The measurement site is located in a unique environment area, with a quite flat landscape, featuring a mix of freshwater and saltwater ecosystems, with the Rhône River flowing into the Mediterranean Sea. The Raman lidar operated almost continuously over the period from 19 October 2022 to 22 February 2024, collecting approximately 12000 hours of lidar measurements (corresponding to ~ 850 Gshots). MARCO, developed by the University of Basilicata, can operate in all weather conditions, with a 24/7 measurement capabilities, with operation being completely remote-controlled. The system relies on a high-power micro-pulse diode-pumped Nd:YAG laser source emitting pulses at 354.7 nm, with a pulse repetition frequency varying within the interval 10–40 kHz. During the present field deployment, the laser was operated at a nominal frequency of 20 kHz, with a single pulse energy of 0.25 mJ and an average emitted power of 5 W. The receiver includes a Ritchey–Chrétien telescope (40 cm diameter primary mirror) and five separate receiving channels including the roto–vibrational Raman backscatter signals from N_2 molecules at

386.7 nm and H_2O molecules at 407.5 nm. Data acquisition is based on the use of transient recorders, with both analogue and digital sampling capabilities. The lidar is compact and easily transportable, being hosted in a sealed and rugged cabinet conceived for outdoor operation in all weather conditions, with the following dimensions: 1.35 m × 1.20 m × 1.73 m (W × D × H). The overall small volume (<3 m^3), weight (750 kg) and power consumption (~900 W) determines a sensitive simplification of the logistics and reduction of costs associated with the transportation and deployment of the system.

No radiosonde launches were available on site. Hence, for the calibration of the system MARCO, radiosondes from the official WMO station of Nîmes-Courbessac have been used. The selected radiosonde launches were identified through air trajectory analysis to maximize airmass coincidence with the lidar site. The statistical uncertainty affecting the measurements was assessed through the application of error propagation techniques to photon-counting signals and to the analogue signals converted into pseudo-photon counts (Di Girolamo et al., 2009). For a temporal resolution of 5 min and a vertical resolution of 100 m, the statistical uncertainty affecting night-time water vapor mixing ratio measurements is approximately 0.3-0.4 g kg^{-1} up to an altitude of 2 km, but performance degrades during the day. The bias affecting water vapor mixing ratio measurements, primarily associated with the calibration of these measurements, is estimated to not exceed 0.2 g kg^{-1}.

A.5 CONCERNING at Toulon (RL6)

In the frame of the WaLiNeAs campaign, the COmpact RamaN lidar for Atmospheric CO_2 and ThERmodyNamic ProfilING (CONCERNING) was deployed at the University of Toulon (Toulon - La Garde, 43.14° N, 6.01° E, 65 m amsl), where it operated almost continuously over the period from 29 September 2022 to 25 January 2023, collecting approximately 2800 hours of lidar measurements (corresponding to almost 1 G laser shots). The area around the measurement site features a hilly and mountainous terrain, with elevations ranging from sea level to several hundred meters. CONCERNING, designed and developed by the University of Basilicata in cooperation with the Institute of Marine Sciences of the Italian National Research Council and the University of Rome “Sapienza” (Di Girolamo et al., 2023a), provides high-resolution profiles of water vapor mixing ratio extending up to the free troposphere, both in daytime and night-time. It was operated during the field deployment with a temporal resolution of 10 s and a vertical resolution of 7.5 m. The receiver includes a Newtonian telescope (50 cm diameter primary mirror) and eight detection channels, two of which are the roto–vibrational Raman backscatter signals from N_2 molecules at 386.7 nm and H_2O molecules at 407.5 nm. CONCERNING uses also rotational Raman channels on O_2 and N_2 molecules. Data acquisition is carried out based on the use of transient recorders, with both an analogue and digital sampling capability. The system is housed in a sealed and rugged cabinet with the following dimensions: 2.60 m × 1.34 m × 2.26 m (W × D × H).

The calibration was carried out based on comparisons with 8 radiosondes launched from “Ile du Levant” (~20 km South-East) and 10 from the WMO station of Nîmes-Courbessac. Comparisons were restricted to the free trophosphere to avoid biases associated with water vapour heterogeneity in the boundary layer. As for the system MARCO, the statistical uncertainty affecting the measurements was calculated through error propagation techniques applied to the photon-counting and analogue signals. For a temporal resolution of 5 min and a vertical resolution of 100 m, the statistical uncertainty affecting water vapor mixing ratio measurements is approximately 0.2 g kg^{-1}, valid up to an altitude of 2 km. The bias affecting water vapor, primarily associated with the calibration of these measurements, is estimated to not exceed 0.1 g kg^{-1}.

A.6 WALI at Cannes (RL7)

The Water Vapour and Aerosol Lidar (WALI, Chazette et al., 2014b; Totems et al., 2021), embedded in the Mobile Atmospheric Station (MAS) (e.g. Raut & Chazette, 2009), has been installed on the Thales Alenia Space site, close to Cannes (43.54° N, 6.96° E, 4 m amsl). The site is located by the sea. The area is characterised by a swift transition from the Mediterranean coastline to the rugged hinterland. The peaks generally reach heights between 300 and 600 m. These include

Mont Vinaigre (approximately 618 m high) to the west of the site and rocky spurs closer to the seashore at altitudes of just a few hundred metres.

The lidar emits an UV pulse energy of ~100 mJ with a repetition rate of 20 Hz at the wavelength of 354.7 nm and fulfils eye-safe conditions. The acquisition was performed for mean profiles of 1000 laser shots leading to a temporal sampling close to 1 minute. The lidar is equipped with six detection channels, which include two channels dedicated to the detection of the water vapor Raman signal at 407.5 nm and the atmospheric nitrogen Raman signal at 386.6 nm (Chazette et al., 2014b). The standard deviation from reference meteorological station is less than 0.25 g kg^{-1} and the absolute deviation is less than 0.4 g kg^{-1}, with a calibration coefficient that remains stable over several years (Chazette et al., 2025). For the inter-comparisons, an averaging time of ±30 minutes, centred on the time value of the IASI profile, has been considered. As for HORUS, the dataset is available as NetCDF files and can be freely downloaded from the AERIS database (https://doi.org/10.25326/537, last access: 31 August 2025). A statistical error profile is provided alongside each WVMR profile.

A.7 ARTHUS at Ajaccio (RL8)

The Atmospheric Raman Temperature and Humidity Sensor (ARTHUS) (Lange et al., 2019) was operated autonomously in Olmeto, Corsica (~25 km south of Ajaccio airport, ~300 m from the coast, 41.70 N, 8.85 E, 20 m amsl) between 16 September and 10 December 2022. It provides, among other atmospheric variables, high-resolution profiles of WVMR from ~200 m above ground level. The raw-data resolution is selectable and was fixed to a temporal resolution of 10 s and a vertical resolution of 7.5 m during WaLiNeAs. The system emits into the atmosphere only eye-safe laser pulses at the third-harmonic radiation of a Nd:YAG laser at a wavelength of about 354.8 nm with a repetition rate of 200 Hz and a pulse energy of ~100 mJ. The first- and second-harmonic wavelength of the laser are separated and blocked. Backscattered signals are collected using a Ritchey–Chrétien–Cassegrain telescope with a 40-cm primary mirror. The receiver separated the elastic and three Raman backscatter signals during WaLiNeAs. In addition to WVMR, ARTHUS measures temperature (rotational Raman Channel on O_2 and N_2), particle backscatter and extinction coefficients simultaneously as well as combined atmospheric variables like relative humidity or lidar ratio. The four-channel receiver is optimized for high efficiency, strong background suppression, and negligible crosstalk from elastic signals with the Raman signals.

For quality control, the statistical uncertainty of the measured data are derived in real-time with Poisson statistics by using the count rates of the photon-counting data (Behrendt et al., 2002, 2004, 2015, 2020; Wulfmeyer et al., 2016). For even better determination of the uncertainties, their total values are derived with an autocorrelation analysis (Lenschow et al., 2000; Behrendt et al., 2015). This technique also allows for distinguishing between uncorrelated instrumental noise and correlated atmospheric variability, enabling the simultaneous retrieval of total uncertainty profiles and higher-order moments of turbulent atmospheric fluctuations, along with their uncertainties (Behrendt et al., 2015, 2020). For temporal averaging of five minutes and vertical averaging over 100 m, the statistical uncertainties in the measured water vapor mixing ratio are typically smaller than 2% up to altitude of 2 km with the exact value depending on the atmospheric transmission, i.e., the aerosol optical depth as well as clouds in the laser path (Lange et al., 2019).

Appendix B: Bias in lidar measurements related to aerosols and temperature

In this appendix the main sources of bias are discussed in relation to the lidar technology described in Appendix A.

B.1 Bias linked to the differential aerosol transmission

This bias is due to the difference in wavelength between the H_2O Raman channel (~407 nm) and the channel used as a reference, which is either a roto–vibrational channel on dinitrogen (N_2) (387 nm) or a rotational channel on dinitrogen and dioxygen ($N_2 + O_2$) (~355 nm).

During the WaLiNeAs field campaign, we observed two contrasting scenarios regarding aerosol loading in the lower and middle troposphere, as recorded by all the lidars. The first scenario corresponds to a typical boundary layer load, with an AOT of less than or around 0.1 at 355 nm. AERONET data (https://aeronet.gsfc.nasa.gov) show variable Ångström exponents of up to ~1.5, averaging around 1. The second scenario is similar to the first, but with the addition of layers of Saharan aerosol plumes, which can lead to AOT of around 0.5 and Ångström exponents of around 0.5 or lower. Based on these two situations, we estimated the bias associated with aerosol-related differential transmission in the lower (≤1.5 km a.m.s.l.) and middle (≥1.5 km a.m.s.l.) tropospheres. The values are shown in Table B1, and the corresponding vertical profiles of bias are given in Figure B1. In the PBL, the bias remains below 0.7% (2%) for lidars using a roto–vibrational (rotational) channel. In the presence of dust aerosol layers, biases of less than 0.5% (1%) can be observed in the PBL and 1.3% (4.7%) in the free troposphere. Above 3 km a.m.s.l., aerosol-related bias significantly influences lidars using a pure rotational channel, where WVMRs predominantly remain below 10 g kg^{-1}.

Table B1: Biases for each Raman lidar due to i) the temperature sensitivity of the backscatter cross section of the H_2O-Raman channel and ii) the differential transmission of aerosols. Two aerosol loads are considered. The first has an aerosol optical thickness (AOT) of 0.1 and an Ångström exponent of 1.5. The second corresponds to the presence of Saharan dust layers, with an AOT of 0.5 and an Ångström exponent of 0.5.

		RL1	RL2	RL3	RL4	RL5	RL6	RL7	RL8
Emitted wavelength (nm)		~354.7	354.69	354.71	354.83	354.72	354.74	354.74	354.70
H_2O-Raman channel									
Central wavelength of filter (CWL) (nm)		407.46	407.56	407.65	407.62	407.50	407.54	407.58	407.5
Filter bandwidth (FWHM) (nm)		1.06	0.30	0.35	0.37	0.25	0.30	0.35	0.30
Bias									
Bias due to aerosols AOT = 0.1 (PBL)		< 0.7%	< 2%	< 0.7%					< 2%
Bias due to aerosols AOT = 0.5 (with dusts)	≤ 1.5 km	< 0.5%	< 1%	< 0.5 %					< 1%
	> 1.5 km	< 1.3%	< 4.7%	< 1.3%					< 4.7 %
Bias due to temperature (ΔT = 30 K)		< 0.3%	2.70%	2.7%	0.5%	2%	1.8%	2.8%	2.2%

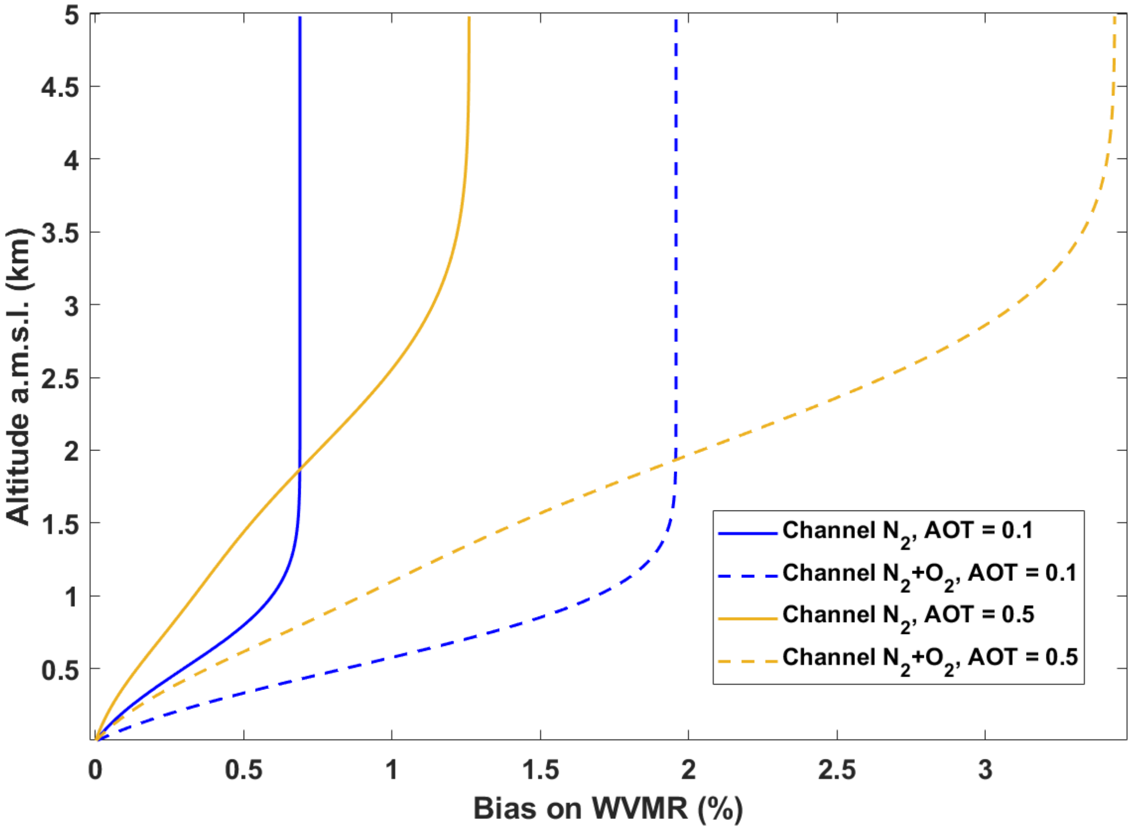

Figure B1: Bias on the lidar-derived water vapor mixing ratio due to the differential aerosol transmission between the water vapor Raman channel and the roto–vibrational nitrogen (N_2) or the rotational (N_2+O_2) channels. Two typical aerosol loads encountered during the field campaign are considered: i) an aerosol optical thickness (AOT) of 0.1 with an Ångström exponent of 1.5 (shown in blue) and ii) an AOT of 0.5 with an Ångström exponent of 0.5 (shown in orange), which corresponds to the presence of dust aerosols.

B.2 Bias linked to the temperature

Lidars are calibrated using radiosondes or ground-based weather stations when equilibrium has been reached in the first few hundred metres of the atmosphere (Laly et al.). The spectral widths of the interferometric filters for the N_2 and N_2+O_2 channels are optimised so that the associated backscattering cross-sections vary little with temperature. The measurements carried out for this article range from the surface to 5 km above mean sea level, with a temperature variation of less than 30°C between these two altitudes. This results in biases of less than 0.15%.

The biases are greater for the H_2O–Raman channel. They are highly dependent on the central wavelength (CWL) of the interference filter used and its full spectral width at half maximum (FWHM). These vary from one lidar to another, as shown in Table A2. Bias calculations were performed based on roto-vibrational Raman spectroscopy of water vapour (Avila et al., 2004; Adam, 2009). The temperature dependence of the Raman backscattering cross-section can be considered linear within a temperature range of 30°C. Biases associated with a temperature variation of 30°C are shown in Table A2. They also vary significantly depending on the lidar but remain below 3%. This is a conservative estimate, as the majority of the data used for this study were collected below 3 km a.m.s.l., and therefore for smaller temperature variations. Furthermore, IASI overpasses occur at fixed times in the morning and evening, with temporal temperature variations remaining below 10°C.

Data availability. The datasets are published open access on the AERIS database (https://en.aeris-data.fr/, last access: 25 November 2025). The IASI products are available at https://data.eumetsat.int/extended?query=iasi# (last access: 3 January 2026). The ERA5 products are available at https://cds.climate.copernicus.eu/datasets (last access: 3 January 2026).

Author contributions. All authors took part in the field campaigns in autumn–winter 2022 and contributed to the data inversion; PC coordinated the field campaign, performed the statistics between lidars, ERA5 and IASI, and wrote the paper. CF coordinated the WaLiNeAs project. AC, PDG, MDP, FL, JT and MS proofread the paper.

Competing interests. The authors declare that they have no conflict of interest.

Acknowledgments. Special thanks to the local authorities of Thales-Alenia-Space, the harbour master of Port Camargue and the Coursan town hall for their welcome during the WaLiNeAs field campaign. The UPC team thanks the technical assistance of Joaquim Giner, Èric Vila and Rubén Tardío. The Spanish groups acknowledge the support of the Ministry for Science and Innovation to ACTRIS ERIC.

Financial support. This research has been supported by the Agence Nationale de la Recherche via the WaLiNeAs project (grant no. ANR-20-CE04-0001). This work was also supported by the French Institut National de l'Univers (INSU) of the Centre National de la Recherche Scientifique (CNRS) and the Commissariat à l'Énergie Atomique et aux Énergies Alternatives (CEA). Funding was also received from the Horizon Europe Programme (project REALISTIC, grant agreement no. 101086690) and from CNES via the EECLAT and AOS projects. The contribution of the University of Basilicata was also funded by the Italian Ministry for Education, University and Research (grants STAC-UP and Tech4You) and the Italian Space Agency (grant CALIGOLA and PROTEO). The contribution of the Universitat de València has been jointly funded by the Spanish Research Agency's (AEI) through the PELICAN project (PID2021-123881OB-I00) and the Valencia Autonomous Government through CIAICO2023-088 project. The contribution of the Universitat Politècnica de Catalunya has been partially supported by the Spanish Research Agency's (AEI) RESA-CI (grant no. PID2019-103886RB-I00) and SYRSAC (grant no. PID2023-149747NB-I00) projects, the Catalan Government through AGAUR (grant no. 2021-SGR-1415) and the European Union through Horizon 2020's ACTRIS IMP (grant no. 871115) and ATMO-ACCESS (grant no. 101008004) projects, and Horizon Europe's REALISTIC project (grant no. 101086690).

6 References

Adam, M.: Notes on temperature-dependent lidar equations, J. Atmos. Ocean. Technol., 26, 1021–1039, https://doi.org/10.1175/2008JTECHA1206.1, 2009.

Amato, U., Antoniadis, A., De Feis, I., Masiello, G., Matricardi, M., and Serio, C.: Technical Note: Functional sliced inverse regression to infer temperature, water vapour and ozone from IASI data, Atmos. Chem. Phys., 9, 5321–5330, https://doi.org/10.5194/acp-9-5321-2009, 2009.

August, T., Klaes, D., Schlüssel, P., Hultberg, T., Crapeau, M., Arriaga, A., O'Carroll, A., Coppens, D., Munro, R., and Calbet, X.: IASI on Metop-A: Operational Level 2 retrievals after five years in orbit, J. Quant. Spectrosc. Radiat. Transf., 113, 1340–1371, https://doi.org/10.1016/j.jqsrt.2012.02.028, 2012.

Avila, G., Fernández, J. M., Tejeda, G., and Montero, S.: The Raman spectra and cross-sections of H2O, D2O, and HDO in the OH/OD stretching regions, J. Mol. Spectrosc., 228, 38–65, https://doi.org/10.1016/j.jms.2004.06.012, 2004.

Behrendt, A., Nakamura, T., Onishi, M., Baumgart, R., and Tsuda, T.: Combined Raman lidar for the measurement of atmospheric temperature, water vapor, particle extinction coefficient, and particle backscatter coefficient, Appl. Opt., 41, 7657, https://doi.org/10.1364/ao.41.007657, 2002.

Behrendt, A., Nakamura, T., and Tsuda, T.: Combined temperature lidar for measurements in the troposphere, stratosphere, and mesosphere, Appl. Opt., 43, 2930–2939, https://doi.org/10.1364/AO.43.002930, 2004.

Behrendt, A., Wulfmeyer, V., Hammann, E., Muppa, S. K., and Pal, S.: Profiles of second- to fourth-order moments of turbulent temperature fluctuations in the convective boundary layer: first measurements with rotational Raman lidar, Atmos. Chem. Phys., 15, 5485–5500, https://doi.org/10.5194/acp-15-5485-2015, 2015.

Behrendt, A., Wulfmeyer, V., Senff, C., Kumar Muppa, S., Späth, F., Lange, Di., Kalthoff, N., and Wieser, A.: Observation of sensible and latent heat flux profiles with lidar, Atmos. Meas. Tech., 13, 3221–3233, https://doi.org/10.5194/amt-13-3221-2020, 2020.

Blanchet, J., Creutin, J. D., and Blanc, A.: Retreating winter and strengthening autumn Mediterranean influence on extreme precipitation in the Southwestern Alps over the last 60 years, Environ. Res. Lett., 16, 034056, https://doi.org/10.1088/1748-9326/abb5cd, 2021.

Boylan, J. W. and Russell, A. G.: PM and light extinction model performance metrics, goals, and criteria for three-dimensional air quality models, Atmos. Environ., 40, 4946–4959, 2006.

Carissimo, A., De Feis, I., and Serio, C.: The physical retrieval methodology for IASI: The δ-IASI code, Environ. Model. Softw., 20, 1111–1126, https://doi.org/10.1016/j.envsoft.2004.07.003, 2005.

Chazette, P., Marnas, F., Totems, J., and Shang, X.: Comparison of IASI water vapor retrieval with H_2O-Raman lidar in the framework of the Mediterranean HyMeX and ChArMEx programs, Atmos. Chem. Phys., 14, 9583–9596, https://doi.org/10.5194/acp-14-9583-2014, 2014a.

Chazette, P., Marnas, F., and Totems, J.: The mobile Water vapor Aerosol Raman LIdar and its implication in the framework of the HyMeX and ChArMEx programs: application to a dust transport process, Atmos. Meas. Tech., 7, 1629–1647, https://doi.org/10.5194/amt-7-1629-2014, 2014b.

Chazette, P., Flamant, C., Raut, J.-C., Totems, J., and Shang, X.: Tropical moisture enriched storm tracks over the Mediterranean and their link with intense rainfall in the Cevennes-Vivarais area during HyMeX, Q. J. R. Meteorol. Soc., 142, https://doi.org/10.1002/qj.2674, 2016.

Chazette, P., Totems, J., and Laly, F.: Long-term evolution of the calibration constant on a mobile/field campaign water vapour Raman lidar, https://doi.org/10.5194/egusphere-2024-3583, January 2025.

Clerbaux, C., Chazette, P., Hadji-Lazaro, J., Mégie, G., Müller, J. F., and Clough, S. A.: Remote sensing of CO, CH4, and O3 using a spaceborne nadir-viewing interferometer, J. Geophys. Res. Atmos., 103, 18999–19013, https://doi.org/10.1029/98JD01422, 1998.

Coopmann, O., Guidard, V., Fourrié, N., Josse, B., and Marécal, V.: Update of Infrared Atmospheric Sounding Interferometer (IASI) channel selection with correlated observation errors for numerical weather prediction (NWP), Atmos. Meas. Tech., 13, 2659–2680, https://doi.org/10.5194/amt-13-2659-2020, 2020.

Cuesta, J., Flamant, C., Gaetani, M., Knippertz, P., Fink, A. H., Chazette, P., Eremenko, M., Dufour, G., Di Biagio, C., and Formenti, P.: Three-dimensional pathways of dust over the Sahara during summer 2011 as revealed by new Infrared Atmospheric Sounding Interferometer observations, Q. J. R. Meteorol. Soc., 146, 2731–2755, https://doi.org/10.1002/qj.3814, 2020.

Divakarla, M., Barnet, C., Goldberg, M., King, T., Maddy, E., Liu, X., Sun, F., Cheng, Z., Gambacorta, A., and Zhou, L.: Validation of AIRS and IASI temperature and water vapor retrievals with global radiosonde measurements and model forecasts, in: Optics InfoBase Conference Papers, HWC5, https://doi.org/10.1364/hisense.2009.hwc5, 2009.

EUMETSAT: IASI All Sky Temperature and Humidity Profiles - Climate Data Record Release 1.1 - Metop-A and -B, https://doi.org/10.15770/EUM_SEC_CLM_0063, 2022.

Flamant, C., Chazette, P., Caumont, O., Di Girolamo, P., Behrendt, A., Sicard, M., Totems, J., Lange, D., Fourrié, N., Brousseau, P., Augros, C., Baron, A., Cacciani, M., Comerón, A., De Rosa, B., Ducrocq, V., Genau, P., Labatut, L., Muñoz-Porcar, C., Rodríguez-Gómez, A., Summa, D., Thundathil, R., and Wulfmeyer, V.: A network of water vapor Raman lidars for improving heavy precipitation forecasting in southern France: introducing the WaLiNeAs initiative, Bull. Atmos. Sci. Technol., 2, https://doi.org/10.1007/s42865-021-00037-6, 2021.

Fouladi, R. T. and Steiger, J. H.: The fisher transform of the pearson product moment correlation coefficient and its square: Cumulants, moments, and applications, Commun. Stat. Simul. Comput., 37, 928–944, https://doi.org/10.1080/03610910801943735, 2008.

Fourrié, N., Nuret, M., Brousseau, P., Caumont, O., Doerenbecher, A., Wattrelot, E., Moll, P., Bénichou, H., Puech, D., Bock, O., Bosser, P., Chazette, P., Flamant, C., Di Girolamo, P., Richard, E., and Saïd, F.: The AROME-WMED reanalyses of the first special observation period of the Hydrological cycle in the Mediterranean experiment (HyMeX), Geosci. Model Dev., 12, 2657–2678, https://doi.org/10.5194/gmd-12-2657-2019, 2019.

Di Girolamo, P., Summa, D., and Ferretti, R.: Multiparameter Raman lidar measurements for the characterization of a dry stratospheric intrusion event, J. Atmos. Ocean. Technol., 26, 1742–1762, https://doi.org/10.1175/2009JTECHA1253.1, 2009.

Di Girolamo, P., Dionisi, D., Cacciani, M., Di Bernardino, A., Franco, N., Summa, D., Di Paolantonio, M., Iannarelli, A. M., and Di Iorio, T.: A Compact Raman Lidar for Atmospheric CO2 and Thermodynamic Profiling: The System CONCERNING, in: Proceedings of the 30th International Laser Radar Conference, 531–537, https://doi.org/10.1007/978-3-031-37818-8_69, 2023a.

Di Girolamo, P., Franco, N., Di Paolantonio, M., Summa, D., and Dionisi, D.: Atmospheric Thermodynamic Profiling through the Use of a Micro-Pulse Raman Lidar System: Introducing the Compact Raman Lidar MARCO, Sensors, 23, 8262, https://doi.org/10.3390/s23198262, 2023b.

Di Girolamo, P., Summa, D., Gandolfi, I., Di Paolantonio, M., Rosoldi, M., De Rosa, B., Dionisi, D., Flamant, C., D'Amico, G., Girolamo, P. Di, Summa, D., Gandolfi, I., Paolantonio, M. Di, Rosoldi, M., Rosa, B. De, Dionisi, D., Flamant, C., and Amico, G. D.: Latent Heat Flux and Turbulent Kinetic Energy Measurements by Lidar in the Frame of the WaLiNeAs Campaign, Remote Sens., 17, 1–19, https://doi.org/10.3390/rs17203473, 2025.

Guidard, V., Fourrié, N., Brousseau, P., and Rabier, F.: Impact of IASI assimilation at global and convective scales and challenges for the assimilation of cloudy scenes, Q. J. R. Meteorol. Soc., 137, 1975–1987, https://doi.org/10.1002/qj.928, 2011.

Guinaldo, T., Voldoire, A., Waldman, R., Saux Picart, S., and Roquet, H.: Response of the sea surface temperature to heatwaves during the France 2022 meteorological summer, Ocean Sci., 19, 629–647, https://doi.org/10.5194/os-19-629-2023, 2023.

Heilliette, S., Rochon, Y. J., Garand, L., and Kaminski, J. W.: Assimilation of infrared radiances in the context of observing system simulation experiments, J. Appl. Meteorol. Climatol., 52, 1031–1045, https://doi.org/10.1175/JAMC-D-12-0124.1, 2013.

Held, I. M. and Soden, B. J.: WATER VAPOR FEEDBACK AND GLOBAL WARMING1, Annu. Rev. Energy Environ., 25, 441–475, https://doi.org/10.1146/annurev.energy.25.1.441, 2000.

Hersbach, H., Bell, B., Berrisford, P., Hirahara, S., Horányi, A., Muñoz-Sabater, J., Nicolas, J., Peubey, C., Radu, R., Schepers, D., Simmons, A., Soci, C., Abdalla, S., Abellan, X., Balsamo, G., Bechtold, P., Biavati, G., Bidlot, J., Bonavita, M., De Chiara, G., Dahlgren, P., Dee, D., Diamantakis, M., Dragani, R., Flemming, J., Forbes, R., Fuentes, M., Geer, A., Haimberger, L., Healy, S., Hogan, R. J., Hólm, E., Janisková, M., Keeley, S., Laloyaux, P., Lopez, P., Lupu, C., Radnoti, G., de Rosnay, P., Rozum, I., Vamborg, F., Villaume, S., and Thépaut, J. N.: The ERA5 global reanalysis, Q. J. R. Meteorol. Soc., 146, 1999–2049, https://doi.org/10.1002/qj.3803, 2020.

Hilton, F., Atkinson, N. C., English, S. J., and Eyre, J. R.: Assimilation of IASI at the Met Office and assessment of its. Impact through observing system experiments, Q. J. R. Meteorol. Soc., 135, 495–505, https://doi.org/10.1002/qj.379, 2009.

Hilton, F., Armante, R., August, T., Barnet, C., Bouchard, A., Camy-Peyret, C., Capelle, V., Clarisse, L., Clerbaux, C., Coheur, P.-F., Collard, A., Crevoisier, C., Dufour, G., Edwards, D., Faijan, F., Fourrié, N., Gambacorta, A., Goldberg, M., Guidard, V., Hurtmans, D., Illingworth, S., Jacquinet-Husson, N., Kerzenmacher, T., Klaes, D., Lavanant, L., Masiello, G., Matricardi, M., McNally, A., Newman, S., Pavelin, E., Payan, S., Péquignot, E., Peyridieu, S., Phulpin, T., Remedios, J., Schlüssel, P., Serio, C., Strow, L., Stubenrauch, C., Taylor, J., Tobin, D., Wolf, W., and Zhou, D.: Hyperspectral Earth Observation from IASI: Five Years of Accomplishments, 2012a.

Hilton, F. I., Newman, S. M., and Collard, A. D.: Identification of NWP humidity biases using high-peaking water vapour channels from IASI, Atmos. Sci. Lett., 13, 73–78, https://doi.org/10.1002/asl.366, 2012b.

IPCC: Climate change 2022: Impacts, Adaptation and Vulnerability. Summary for policymakers. Contribution of Working Group II to the Sixth Assessment Report of the Intergovernmental Panel on Climate Change, in: United Nations Environment Programme UNEP, vol. AR6, Cambridge University Press, 551–712, 2022.

Klaes, K. D., Cohen, M., Buhler, Y., Schlüssel, P., Munro, R., Luntama, J.-P., von Engeln, A., Clérigh, E. Ó., Bonekamp, H., Ackermann, J., and Schmetz, J.: An Introduction to the EUMETSAT Polar system, Bull. Am. Meteorol. Soc., 88, 1085–1096, https://doi.org/10.1175/BAMS-88-7-1085, 2007.

Kumar, D., Rocadenbosch, F., Sicard, M., Comeron, A., Muñoz, C., Lange, D., Tomás, S., and Gregorio, E.: Six-channel polychromator design and implementation for the UPC elastic/Raman lidar, in: Lidar Technologies, Techniques, and Measurements for Atmospheric Remote Sensing VII, 81820W, https://doi.org/10.1117/12.896305, 2011.

Lacour, J. L., Risi, C., Worden, J., Clerbaux, C., and Coheur, P. F.: Importance of depth and intensity of convection on the isotopic composition of water vapor as seen from IASI and TES δD observations, Earth Planet. Sci. Lett., 481, 387–394, https://doi.org/10.1016/j.epsl.2017.10.048, 2018.

Laly, F. and Chazette, P.: Comparative analysis of ERA5 and Raman lidar-derived moisture profiles in the framework of the WaLiNeAs field campaigns, Q. J. R. Meteorol. Soc., e5044, https://doi.org/10.1002/qj.5044, 2025.

Laly, F., Chazette, P., Totems, J., Lagarrigue, J., Forges, L., and Flamant, C.: Water vapor Raman-lidar observations from multiple sites in the framework of WaLiNeAs, Earth Syst. Sci. Data, 16, 5579–5602, https://doi.org/10.5194/ESSD-16-5579-2024, 2024.

Lange, D., Behrendt, A., and Wulfmeyer, V.: Compact Operational Tropospheric Water Vapor and Temperature Raman Lidar with Turbulence Resolution, Geophys. Res. Lett., 46, 14844–14853, https://doi.org/10.1029/2019GL085774, 2019.

Lenschow, D. H. H., Wulfmeyer, V., and Senff, C.: Measuring second through fourth-order moments in noisy data, J. Atmos. Ocean. Technol., 17, 1330–1347, https://doi.org/https://doi.org/10.1175/1520-0426(2000)017<1330:MSTFOM>2.0.CO;2, 2000.

Masiello, G., Serio, C., Deleporte, T., Herbin, H., Di Girolamo, P., Champollion, C., Behrendt, A., Bosser, P., Bock, O., Wulfmeyer, V., Pommier, M., and Flamant, C.: Comparison of IASI water vapour products over complex terrain with COPS campaign data, Meteorol. Zeitschrift, 22, 471–487, https://doi.org/10.1127/0941-2948/2013/0430, 2013.

Matricardi, M. and Mcnally, A. P.: The direct assimilation of principal components of IASI spectra in the ECMWF 4D-Var, Q. J. R. Meteorol. Soc., 140, 573–582, https://doi.org/10.1002/qj.2156, 2014.

Pérez, C., Sicard, M., Jorba, O., Comerón, A., and Baldasano, J. M.: Summertime re-circulations of air pollutants over the north-eastern Iberian coast observed from systematic EARLINET lidar measurements in Barcelona, Atmos. Environ., 38, 3983–4000, https://doi.org/10.1016/j.atmosenv.2004.04.010, 2004.

Pougatchev, N., August, T., Calbet, X., Hultberg, T., Oduleye, O., Schlüssel, P., Stiller, B., Germain, K. St., Bingham, G., St Germain, K., and Bingham, G.: IASI temperature and water vapor retrievals - Error assessment and validation, Atmos. Chem. Phys. Discuss., 9, 7971–7989, https://doi.org/10.5194/acpd-9-7971-2009, 2009.

Randriamiarisoa, H., Chazette, P., Couvert, P., Sanak, J., and Mégie, G.: Relative humidity impact on aerosol parameters in a Paris suburban area, Atmos. Chem. Phys., 6, 1389–1407, https://doi.org/10.5194/acp-6-1389-2006, 2006.

Ricard, D., Ducrocq, V., and Auger, L.: A climatology of the mesoscale environment associated with heavily precipitating events over a northwestern Mediterranean area, J. Appl. Meteorol. Climatol., 51, 468–488, https://doi.org/10.1175/JAMC-D-11-017.1, 2012.

Rood, M. J., Covert, D. S., and Larson, T. V: Hygroscopic properties of atmospheric aerosol in Riverside, California, Tellus B, 39, https://doi.org/10.3402/tellusb.v39i4.15357, 1987.

De Rosa, B., Di Girolamo, P., and Summa, D.: Temperature and water vapour measurements in the framework of the Network for the Detection of Atmospheric Composition Change (NDACC), Atmos. Meas. Tech., 13, 405–427, https://doi.org/10.5194/AMT-13-405-2020, 2020.

Schlüssel, P., Hultberg, T. H., Phillips, P. L., August, T., and Calbet, X.: The operational IASI Level 2 processor, in: Advances in Space Research, 982–988, https://doi.org/10.1016/j.asr.2005.03.008, 2005.

Schneider, M., Romero, P. M., Hase, F., Blumenstock, T., Cuevas, E., and Ramos, R.: Continuous quality assessment of atmospheric water vapour measurement techniques: FTIR, Cimel, MFRSR, GPS, and Vaisala RS92, Atmos. Meas. Tech., 3, 323–338, https://doi.org/10.5194/amt-3-323-2010, 2010.

Stuart, A. and Ord, J. K.: Kendall's Advanced Theory of Statistics, Edward Arn., London-Melbourne-Auckland, 1991.

Tombette, M., Chazette, P., Sportisse, B., and Roustan, Y.: Simulation of aerosol optical properties over Europe with a 3-D size-resolved aerosol model: comparisons with AERONET data, Atmos. Chem. Phys., 8, 7115–7132, https://doi.org/10.5194/acp-8-7115-2008, 2008.

Whiteman, D. N.: Examination of the traditional Raman lidar technique I Evaluating the temperature-dependent lidar equations, Appl. Opt., 42, 2571, https://doi.org/10.1364/AO.42.002571, 2003.

Wulfmeyer, V., Muppa, S. K., Behrendt, A., Hammann, E., Späth, F., Sorbjan, Z., Turner, D. D., and Hardesty, R. M.: Determination of convective boundary layer entrainment fluxes, dissipation rates, and the molecular destruction of variances: Theoretical description and a strategy for its confirmation with a novel lidar system synergy, J. Atmos. Sci., 73, 667–692, https://doi.org/10.1175/JAS-D-14-0392.1, 2016.

Xu, D., Liu, Z., Huang, X. Y., Min, J., and Wang, H.: Impact of assimilating IASI radiance observations on forecasts of two tropical cyclones, Meteorol. Atmos. Phys., 122, 1–18, https://doi.org/10.1007/s00703-013-0276-2, 2013.

Zhou, D. K., Smith, W. L., Larar, A. M., Liu, X., Taylor, J. P., Schlüssel, P., Strow, L. L., and Mango, S. A.: All weather IASI single field-of-view retrievals: Case study - Validation with JAIVEx data, Atmos. Chem. Phys., 9, 2241–2255, https://doi.org/10.5194/acp-9-2241-2009, 2009.